Electroproduction of the $S_{11}(1535)$ Resonance at High Momentum Transfer

C. S. Armstrong^{2*}, P. Stoler⁷, G. S. Adams⁷, A. Ahmidouch^{3,4}, K. Assamagan³, S. Avery³, O. K. Baker^{3,8}, P. Bosted¹, V. Burkert⁸, R. Carlini⁸, J. Dunne⁸, T. Eden³, R. Ent⁸, V. V. Frolov^{7,†}, D. Gaskell³, P. Guèye³, W. Hinton³, C. Keppel^{3,8}, W. Kim⁵, M. Klusman⁷, D. Koltenuk⁹, D. Mack⁸, R. Madey^{3,4}, D. Meekins², R. Minehart¹⁰, J. Mitchell⁸, H. Mkrtchyan¹¹, J. Napolitano⁷, G. Niculescu³, I. Niculescu³, M. Nozar⁷, J. W. Price^{7,‡}, V. Tadevosyan¹¹, L. Tang^{3,8}, M. Witkowski⁷, S. Wood⁸

¹ Physics Department, American University, Washington D.C. 20016, USA
 ² Department of Physics, College of William & Mary, Williamsburg, VA 23187, USA
 ³ Physics Department, Hampton University, Hampton, VA 23668, USA
 ⁴ Physics Department, Kent State University, Kent, OH 44242, USA
 ⁵ Physics Department, Kyungpook National University, Taegu, South Korea
 ⁷ Physics Department, Rensselaer Polytechnic Institute, Troy, NY 12180, USA
 ⁸ Thomas Jefferson National Accelerator Facility, Newport News, VA 23606, USA
 ⁹ Physics Department, University of Pennsylvania, Philadelphia, PA 19104, USA
 ¹⁰ Physics Department, University of Virginia, Charlottesville, VA 22903, USA
 ¹¹ Yerevan Physics Institute, Yerevan, Armenia

(September 18, 2018)

The differential cross section for the process $p(e,e'p)\eta$ has been measured at $Q^2=2.4$ and 3.6 $(\text{GeV}/c)^2$ at center-of-mass energies encompassing the $S_{11}(1535)$ resonance. The latter point is the highest- Q^2 exclusive measurement of this process to date. The resonance width and the helicity-1/2 transition amplitude are extracted from the data, and evidence for the possible onset of scaling in this reaction is shown. A lower bound of ≈ 0.45 is placed on the $S_{11}(1535) \rightarrow p\eta$ branching fraction.

PACS Numbers: 13.60.Rj, 13.40.Gp, 13.60.Le, 14.20.Gk

I. INTRODUCTION

Baryon electroproduction allows the measurement of transition form factors, which test models of hadronic structure in ways that static baryon properties alone cannot. Recently much effort has gone into attempts to reproduce observed transition form factors over a large range of four-momentum transfer. At low four-momentum transfer, or Q^2 , the focus has been on incorporating relativistic effects into the constituent quark model (CQM) [1], using light-front [2–4] and other [5,6] approaches. At higher Q^2 , perturbative QCD (pQCD) sum rule calculations [7] and valence pQCD [8] have been employed. The applicable range in Q^2 for these various approaches is not clear.

Among the most interesting of baryon case studies is the $S_{11}(1535)$ resonance, which is one of the most strongly excited states over all Q^2 , and which is easily isolated because it is the only resonance that has a large branching fraction to the η . The reproduction of the $S_{11}(1535)$ form factor has become a goal of many models, but the effort has been hampered by a lack of precise electroproduction data. In addition, the uncer-

tainty in the $S_{11}(1535)$ transition amplitude is limited by knowledge of the full width and branching fraction to the η . We report here on a measurement of the reaction $e + p \rightarrow e' + S_{11}(1535) \rightarrow e' + p + \eta$ and an extraction of the helicity-conserving transition amplitude $A_{1/2}^p$ at $Q^2 = 2.4$ and 3.6 (GeV/c)². We also use a recent analysis of inclusive (e, e') data to put a lower bound on the $S_{11}(1535) \rightarrow p \eta$ branching fraction.

II. THE EXPERIMENT

The experiment was performed in Hall C of the Thomas Jefferson National Accelerator Facility (Jefferson Lab), shown in Figure 1. The Short Orbit Spectrometer (SOS), which is a resistive $QD\bar{D}$ device, was used to detect electrons. The High Momentum Spectrometer (HMS), which is a superconducting QQQD spectrometer, was used to detect protons. Figure 2 shows the HMS detectors, which include drift chambers (DC1 and DC2) for determining track information, scintillator arrays (S1X/Y and S2X/Y) for triggering and time-of-flight measurement, and a threshold gas Čerenkov and electromagnetic calorimeter for particle identification (PID). The SOS detectors are configured similarly.

The incident electrons had energies E=3.245 and $4.045~{\rm GeV}$ for the $Q^2=2.4$ and $3.6~({\rm GeV}/c)^2$ points, respectively. At each of the two Q^2 points, the electron spectrometer was fixed in angle and momentum, thus defining a central three-momentum transfer ${\bf q}$ and direction of a boosted decay cone of protons. The proton spectrometer was stepped in angle and in momentum to capture as much of this decay cone as possible. Data were obtained at 33 (21) kinematic settings at the low (high) Q^2 point.

Target protons were provided in the form of liquid hydrogen at 19 K flowing through a target of length

4.36 cm. The relative current of the electron beam was measured by two resonant-cavity current monitors, which were calibrated periodically using the absolute beam current measurement of a parametric current transformer. The combined measurement had an absolute accuracy of $\sigma = 1.5\%$.

Electrons were identified in the SOS using the Čerenkov detector and lead-glass calorimeter (see Figure 3). In the HMS, protons were separated from pions using the time of flight measured between two pairs of scintillator arrays (see Figure 4). In both spectrometers, tracking information was obtained from the drift chambers. Details of the experiment and analysis are given in Ref. [9], and information on a simultaneous measurement of the $\Delta(1232)$ can be found in Ref. [10].

III. DATA ANALYSIS

The data were corrected for trigger and PID inefficiencies (< 1%), track reconstruction inefficiencies ($\approx 5\%$), computer and electronic dead times (< 5%), current-dependent target density changes ($\approx 3\%$), and protons undetected due to interactions in the detector stack ($\approx 3\%$). The data were binned in W, $\cos \theta_{\eta}^*$, ϕ_{η}^* , and M_x^2 (with 6, 10, 6, and 20 bins, respectively). Here W is the invariant mass; θ_{η}^* is the polar angle between the direction of the η and the three-momentum transfer ${\bf q}$ in the center-of-mass (c.m.) of the resonance; ϕ_{η}^* is the azimuthal angle of the η with respect to the electron scattering plane; and M_x^2 is the square of the missing mass for p(e,e'p)X. The η mesons were identified in the final state using M_x^2 . Figure 5 shows the missing mass distribution for a typical kinematic setting.

Modest backgrounds in M_x^2 due to accidentals ($\approx 2\%$ shown in Figure 4) and protons penetrating the HMS collimator and magnet apertures ($\approx 4\%$) were measured and subtracted from the data. The remaining continuum background in missing mass was due to multi-pion $(n\pi)$ production (ranging from 30% to 50% of the resonance data) and a small (< 2%) contribution from targetwindow interactions. Two independent techniques were used to subtract these remaining background events. The first technique fitted a polynomial plus peak in ${\cal M}_x^2$ to the data in each $(\cos \theta_{\eta}^*, \phi_{\eta}^*)$ bin (integrated over the W acceptance for that kinematic setting), and then subtracted the background contribution from each bin. The second technique scaled a Monte Carlo-generated $n\pi$ background to match the data above and below the missingmass peak and then subtracted this background from each $(W, \cos \theta_n^*, \phi_n^*)$ bin.

Three different models were used to simulate the $n\pi$ background in the Monte Carlo: $e\,p \to e'\,p\,\pi^+\,\pi^-$, $e\,p \to e'\,\Delta^{++}\,\pi^- \to e'\,p\,\pi^+\,\pi^-$, and a crude approximation of three-body phase space. The Monte Carlo simulation was also used to simulate multiple scattering and ionization energy loss, and to correct for experimental acceptance

and the effect of radiative processes. Once the $n\pi$ background was subtracted from both experimental and simulated spectra, the experimental yields were corrected to account for finite Q^2 acceptance. The differential cross section was then given by the ratio of experimental to simulated yield in each $(W, \cos\theta^*_{\eta}, \phi^*_{\eta})$ bin, normalized by the simulation resonance cross section for that bin.

The cross sections obtained using the different $n\pi$ models and the two background subtraction techniques all agreed within 2%; both the following figures and our final results were obtained using the first subtraction technique together with a background generated by combining two of the $n\pi$ models. Figure 6 shows data and fits for several typical $(\cos\theta^*_{\eta}, \phi^*_{\eta})$ bins of one kinematic settings. Figure 7 shows the result of fits for several kinematic settings, where for each setting we have integrated both the data and their respective fits over the sixty individual $(\cos\theta^*_{\eta}, \phi^*_{\eta})$ bins.

Using similar techniques we verified the well-known ${}^{1}\mathrm{H}(\mathrm{e},\mathrm{e'p})$ cross section [11] to within 2%.

IV. RESULTS

The five-fold differential cross section for the $ep \to e'p\eta$ process may be expressed as the product of the transverse virtual photon flux Γ_T (Hand convention [12]) and the c.m. cross section for the electroproduction of the $p\eta$ pair:

$$\frac{d\sigma}{d\Omega_e dE'_e d\Omega^*_{\eta}} = \Gamma_T \frac{d\sigma}{d\Omega^*_{\eta}} \left(\gamma_v \, p \to p \, \eta \right) \,. \tag{1}$$

Previous data indicate that the c.m. $\gamma_v p \to p \eta$ cross section is dominated by S-waves arising from the $S_{11}(1535)$ [13,14]. This dominance was confirmed by the present data, which showed that terms other than S-wave were less than 7% and consistent with zero within the statistical uncertainty of the data. Angular distributions for the $Q^2=3.6~({\rm GeV}/c)^2$ data are shown in Figure 8.

From S-wave fits to the angular distributions, the total cross section was calculated (at each Q^2 point) as a function of W:

$$\sigma_{\rm tot}(W) = 4\pi \frac{d\sigma}{d\Omega_n^*} (\gamma_v p \to p\eta) \ .$$
 (2)

This cross section, which consists of resonant and nonresonant parts, was fitted with a relativistic Breit-Wigner plus nonresonant background curve,

$$\sigma_{\text{tot}}(W) = \sigma_{\text{res}}(W) + \sigma_{\text{nr}}(W)$$

$$= A_{\text{res}}^2 \frac{|\mathbf{p}_{\eta}^*| W}{m_p K} \frac{W_R^2 \Gamma_R^2}{(W^2 - W_R^2)^2 + W_R^2 \Gamma^2(W)}$$

$$+ B_{\text{nr}} \sqrt{W - W_{\text{thr}}} , \qquad (3)$$

where W_R is the resonance mass, Γ_R is the full width, $A_{\rm res}^2$ and $B_{\rm nr}$ are the Q^2 -dependent magnitudes of the

resonant and nonresonant terms, K is the equivalent real photon energy $[K = (W^2 - m_p^2)/(2m_p)]$, and \mathbf{p}_{η}^* is the three-momentum of the η in the c.m. of the $p\eta$ system. The $p\eta$ production threshold is at $W_{\rm thr} \approx 1486$ MeV (in the lowest W bin). At both values of Q^2 , the fitted value of the phenomenological nonresonant term $(B_{\rm nr} \sqrt{W - W_{\rm thr}})$ was consistent with zero (with an uncertainty of 1% of the resonant term).

The energy-dependent resonance width $\Gamma(W)$ of Eq. 3 was parameterized in terms of the branching fractions b_{η} ($\equiv \Gamma_{\eta}/\Gamma_R$ at W_R), b_{π} , and $b_{\pi\pi}$ according to Walker [15]. At present the Particle Data Group (PDG) gives an estimated range for the η branching fraction of $0.30 \leq b_{\eta} \leq 0.55$ [16]. Therefore, fits to $\sigma_{\rm res}(W)$ were made assuming three sets of values for the branching fractions ($b_{\eta}:b_{\pi}:b_{\pi\pi}$), which we define as Fits 1–3, respectively: (0.55:0.35:0.10), (0.45:0.45:0.10), and (0.35:0.55:0.10). A consequence of the $p\eta$ threshold is that the fit to $\sigma_{\rm res}(W)$ cannot constrain the branching fractions [9] (i.e., the three fits result in curves that are virtually indistinguishable).

Based on a branching fraction constraint presented below, we consider Fit 1 ($b_{\eta} = 0.55$) to $\sigma_{\rm res}(W)$ to be the preferred fit. The fits for both Q^2 points are shown in Figure 9. With the Fit 1 branching fractions, we obtain a full width $\Gamma_R = (154 \pm 20)$ MeV. This width changed less than 10 MeV over the range of branching fraction assumptions. The uncertainty is statistical added in quadrature with systematic. Our result agrees with the PDG estimate ($\approx 150 \text{ MeV}$) [16], and appears lower than the recent Mainz measurement, $\Gamma_R = (203\pm35) \text{ MeV } [13]$ (see inset of Figure 9). These recent results disagree with the value of $\Gamma_R = (68 \pm 7)$ MeV obtained from the high- Q^2 measurement of Ref. [14]. The form of the Breit-Wigner parameterization used by the three groups is essentially the same, and so does not account for the differences in Γ_R .

As noted above, the fit to $\sigma_{\rm res}(W)$ cannot constrain the branching fraction b_{η} , but a comparison between this work and a recent fit to inclusive (e,e') scattering [17] can. The fit by Keppel *et al.* models the inclusive cross section in terms of transverse resonant $(\sigma_{T_{res}})$ and nonresonant $(\sigma_{T_{nr}})$ contributions using

$$\frac{d\sigma}{d\Omega_e dE'_e} = \Gamma_T \left[\sigma_{T_{nr}} \left(1 + \varepsilon R_{nr} \right) + \sigma_{T_{res}} \right]. \tag{4}$$

In that work, the resonant contribution from each of the three resonance regions (assumed to be entirely transverse) is fit using a Breit-Wigner form. The transverse component of the nonresonant contribution is fit using the phenomenological form

$$\sigma = \sum_{n=1}^{3} C_n(Q^2) (W - W_{\text{thr}})^{n - \frac{1}{2}}, \qquad (5)$$

where the $C_n(Q^2)$ are fourth-order polynomials in Q^2 . The longitudinal component of the nonresonant cross section, which enters through the longitudinal-to-transverse ratio R_{nr} , is taken from a fit to deep inelastic data [18].

The resonant part of the second resonance region is dominated at low Q^2 by the $D_{13}(1520)$. At higher Q^2 , however, the $S_{11}(1535)$ begins to dominate, and by $Q^2 = 4 \text{ (GeV/}c)^2$ it is expected that the $S_{11}(1535)$ is responsible for over 90% of the resonant cross section at $W \approx 1535 \text{ MeV } [14]$. Assuming that the resonant part of the inclusive cross section is the incoherent sum of the resonant contributions of the various decay channels, we can use the inclusive and exclusive resonant cross sections to put a lower bound on b_n [9]:

$$b_{\eta} \ge \frac{\sigma_{\rm res}(S_{11} \to p \, \eta)}{\sigma_{\rm res}(\text{inclusive})} \,,$$
 (6)

where both cross sections are taken at $W \approx 1535$ MeV. A value of $b_{\eta} = 0.55$ results in good agreement between the high- Q^2 point of this work and the inclusive fit; a value of $b_{\eta} = 0.35$, on the other hand, implies an inclusive cross section 50% greater than the fit to the measured inclusive cross section, which is strong evidence that the branching fraction is not this low. With the incoherent summation ansatz given above, and assigning a 10% uncertainty to the inclusive fit, we find a lower bound of $b_{\eta} = 0.45$ with a 95% confidence level. Assuming complete S_{11} dominance at $Q^2 = 4.0$ (GeV/c)², we find a best fit of $b_{\eta} = 0.55$.

Neglecting resonances other than the $S_{11}(1535)$, we relate the amplitude $A_{1/2}^p$ to $\sigma_{\rm res}$ by [13,19]

$$A_{1/2}^{p}(Q^{2}) = \left[\frac{W_{R} \Gamma_{R}}{2 m_{p} b_{\eta}} \frac{\sigma_{\text{res}}(Q^{2}, W_{R})}{1 + \varepsilon R} \right]^{1/2} . \tag{7}$$

Here ε is the longitudinal polarization of the virtual photon, and $R = \sigma_L/\sigma_T$. For R we assumed a parameterization based on a quark-model calculation [20]. The expected impact of the longitudinal-to-transverse ratio R on the final physics result is small: a 100% error in the assumed value [$\approx 4\%$ at $Q^2 = 2.4~({\rm GeV}/c)^2$] corresponds to an uncertainty of less than 1% in the quoted value of $A_{1/2}^p$.

Table I gives final results for Fits 1–3. The uncertainties are systematic and statistical added in quadrature; for $A_{1/2}^p$ we included estimates for the uncertainties from Γ_R and b_{η} , which were obtained by varying these quantities over reasonable ranges (150–200 MeV and 0.45–0.6, respectively) and studying the effect on the helicity amplitude.

Table II lists the dominant sources of systematic uncertainty in the measurement and their impact on the differential cross section and on the helicity amplitude. The uncertainty in $\frac{d^2\sigma}{d\Omega_{\eta}^*}$ is given as a range, where the largest uncertainties are for the highest W bins.

Figure 10 shows the helicity amplitude results, along with points calculated from previous $e\,p \to e'p\,\eta$ data and some theoretical predictions. All data points in the figure were calculated using Eq. 7 assuming $\Gamma_R=154~{\rm MeV}$

TABLE I. Results. The uncertainties are systematic (including estimated uncertainties in Γ_R and b_η for $A_{1/2}^p$) and statistical added in quadrature. The top $A_{1/2}^p$ result is for $Q^2=2.4~({\rm GeV}/c)^2$, the bottom is for $Q^2=3.6~({\rm GeV}/c)^2$. Fit 1 is preferred for reasons discussed in the text. The 'best value' for b_η assumes S_{11} dominance at $Q^2=4~({\rm GeV}/c)^2$.

Quantity	Fit 1	Fit 2	Fit 3
$W_R [\text{MeV}]$	1532 ± 5	1527 ± 5	1521 ± 5
$\Gamma_R \; [{ m MeV}]$	154 ± 20	150 ± 19	147 ± 19
$A_{1/2}^p [10^{-3} \text{ GeV}^{-1/2}]$	50 ± 7	55 ± 8	63 ± 9
$A_{1/2}^{p} [10^{-3} \text{ GeV}^{-1/2}]$	35 ± 5	39 ± 6	44 ± 6
$b_{\eta} = \Gamma_{\eta}/\Gamma_{R}$	> 0.45 ; best value ≈ 0.55		

TABLE II. Dominant sources of systematic uncertainty, not including Γ_R and b_η (which affect $A_{1/2}^p$).

	Fractional uncertainty (σ) in	
Quantity	$\frac{d^2\sigma}{d\Omega_{\eta}^*}$	$A_{1/2}^{p}$
Monte Carlo $n\pi$ model	1% to $7%$	1%
$n\pi$ subtraction	1% to $6%$	1%
Knowledge of E	1% to $10%$	0.8%
Knowledge of θ_e	0.2% to $11%$	1%
Experimental Acceptance	1% to $6%$	1%

and $b_{\eta}=0.55$; if either assumption is wrong, all data points will scale together. Not included for any of the data points in the figure are the uncertainties in Γ_R and b_{η} . Note the good agreement between the high- Q^2 point of the present work and the inclusive fit for $b_{\eta}=0.55$; assumption of a lower branching fraction shifts the data up relative to the inclusive fit.

The present result differs from previous work in both the strength and the slope of the $S_{11}(1535)$ form factor; most notably, we find a cross section 30% lower than that of Ref. [14] [found by interpolating the results of this work to $Q^2 = 3$ (GeV/c)²]. This difference is reduced in the amplitude by the square root relating $A_{1/2}^p$ to the cross section (Eq. 7). Although the present data were taken at a different value of ε than those of Ref. [14], a longitudinal cross section is not responsible for the difference between the two measurements; a value of $R \approx 2.3$ (which is ruled out at low Q^2 [21,22]) would be necessary to account for the discrepancy.

Of the various CQM curves shown in Figure 10, none exhibit a slope as shallow as that of the data. Those that indicate an amplitude at $Q^2 \sim 3 \text{ (GeV/}c)^2$ roughly consistent with experimental data also predict excess amplitude at lower Q^2 . Our data also have consequences for a recent coupled-channel model for the $S_{11}(1535)$ [27]; the proposed quasi-bound $K\Sigma$ (five quark) state is expected to have a form factor that decreases more rapidly than is observed.

Figure 11 shows the quantity $Q^3 A_{1/2}^p$ for the $S_{11}(1535)$, which is predicted by pQCD to asymptotically approach a constant at high Q^2 [7]. As has been pointed out else-

where [28], such scaling might be due to non-perturbative contributions. While there is no *strong* scaling evident in the figure, our data indicate that $Q^3A_{1/2}^p$ may be approaching a constant value by $Q^2 \sim 5 \text{ (GeV/}c)^2$.

V. CONCLUSIONS

We have presented the results of a precise, high statistics measurement of the $ep \rightarrow e'p\eta$ process at $W \approx 1535$ MeV and at $Q^2 = 2.4$ and 3.6 (GeV/c)² [29]. The contribution of terms other than S-wave multipoles is observed to be less than 7%, which is consistent with previous measurements. More importantly, the cross section obtained from the new data is about 30% lower and indicates a full width twice that of the only other exclusive measurement at comparable Q^2 [14].

While the new data exhibit no strong perturbative signature, they do have a Q^2 dependence that is markedly different than the older high- Q^2 measurement. Even given the new (lower) cross section obtained from this measurement, however, relativized versions of the quark model fail to reproduce the Q^2 dependence seen experimentally.

A comparison of the new high- Q^2 datum (the highest in existence) with a recent inclusive analysis indicates an $S_{11}(1535) \to p\,\eta$ branching fraction of at least $b_\eta = 0.45$. Using $b_\eta = 0.55$ we obtain $\Gamma_R = 154$ MeV and a new measurement of $A^p_{1/2}(Q^2)$ (see Table I).

We wish to acknowledge the support of those in the Jefferson Lab accelerator division for their invaluable work during the experiment. This work was supported in part by the U. S. Department of Energy and the National Science Foundation. CSA also thanks SURA and Jefferson Lab for their support.

- * Present address: Thomas Jefferson National Accelerator Facility, Newport News, VA 23606, USA. Email: csa@jlab.org.
- † Present address: University of Minnesota, Minneapolis, MN, 55455.
- Present address: Physics Program, Louisiana Tech University, Ruston, LA 71272.
- [1] N. Isgur and G. Karl, Phys. Lett. **72B**, 109 (1977); Phys. Lett. **74B**, 353 (1978).
- [2] S. Capstick and B. D. Keister, Phys. Rev. D 51, 3598 (1995).
- [3] This is a calculation in the light-front model of Ref. [2], which assumes pointlike quarks and simple wavefunctions, but (in contrast to the published work) uses the standard convention for the normalization of states, and a different method for extraction of helicity amplitudes, along with numerical improvements. This effort is on-

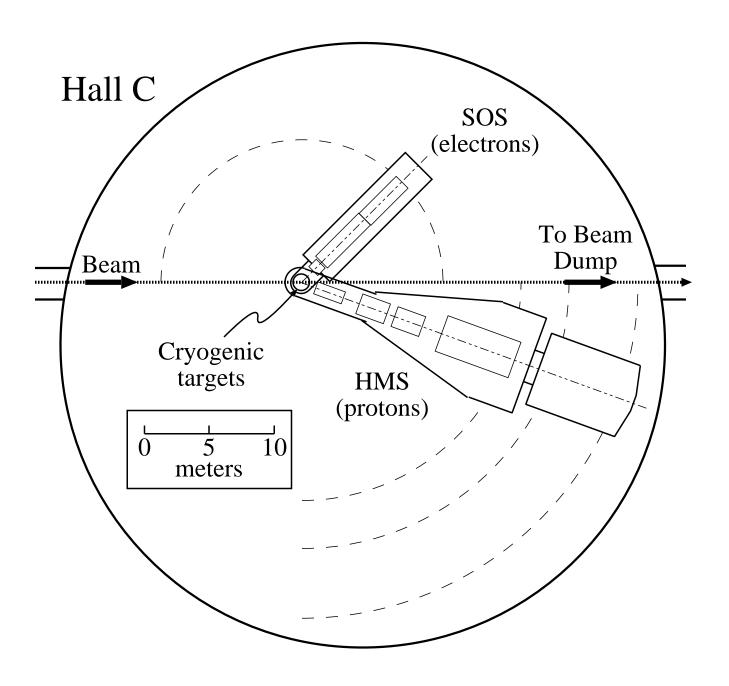
- going at the time of this writing. S. Capstick, personal communication (1998).
- [4] R. Stanley and H. Weber, Phys. Rev. C 52, 435 (1995).
- [5] Z. Li and F. Close, Phys. Rev. D 42, 2207 (1990).
- [6] M. Warns et al., Z. Phys. C45, 613 (1990); Z. Phys. C45, 627 (1990); Phys. Rev. D 42, 2215 (1990).
- [7] C. E. Carlson and J. L. Poor, Phys. Rev. D 38, 2758 (1988).
- [8] D. B. Leinweber, T. Draper, and R. M. Woloshyn, Phys. Rev. D 46, 3067 (1992).
- [9] C. S. Armstrong, Ph.D. dissertation, College of William & Mary (unpublished) (1998).
- [10] V. V. Frolov et al., Phys. Rev. Lett. 82, 45 (1999);
 V. V. Frolov, Ph.D. dissertation, Rensselaer Polytechnic Institute (unpublished) (1998).
- [11] The Monte Carlo simulation of ${}^{1}\text{H}(e,e'p)$ used the dipole form factor $(1+Q^2/0.71)^{-2}$ for G_{E_p} , and the Gari-Krümpelmann parameterization for G_{M_p} [M. Gari and W. Krümpelmann, Z. Phys. **A322**, 689 (1985)].
- [12] L. N. Hand, Phys. Rev. 129, 1834 (1963).
- [13] B. Krusche et al., Phys. Rev. Lett. **74**, 3736 (1995).
- [14] F. Brasse et al., Z. Phys. **C22**, 33 (1984).
- [15] R. L. Walker, Phys. Rev. **182**, 1729 (1969).
- [16] C. Caso et al., European Physical Journal C3, 1 (1998).
- [17] C. Keppel, Workshop on CEBAF at Higher Energies, Newport News, 1994, edited by N. Isgur and P. Stoler, and C. Keppel, Ph.D. dissertation, The American University (unpublished) (1994). This is a global fit to SLAC resonance electroproduction data. It is similar to earlier work done by Bodek [A. Bodek, Phys. Rev. D 20, 1471 (1979)] and Stoler [P. Stoler, Phys. Rev. Lett. 66, 1003 (1991); Phys. Rev. D 44, 73 (1991)]. A similar fit, but to a reduced data set, is found in L. M. Stuart, et al., Phys. Rev. D58, 032003 (1998). In the kinematic region of the present work, the Keppel and Stuart fits are in agreement at the 2% level.
- [18] L. W. Whitlow et al., Phys. Lett. 250B, 193 (1990).
- [19] Particle Data Group, Rev. Mod. Phys. 48, S157 (1976).
- [20] F. Ravndal, Phys. Rev. D 4, 1466 (1971).
- [21] H. Breuker et al., Phys. Lett. **74B**, 409 (1978).
- [22] F. Brasse et al., Nucl. Phys. B139, 37 (1978).
- [23] P. Kummer et al., Phys. Rev. Lett. 30, 873 (1973).
- [24] U. Beck et al., Phys. Lett. **51B**, 103 (1974).
- [25] J. Alder et al., Nucl. Phys. **B91**, 386 (1975).
- [26] M. Aiello, M. M. Giannini, and E. Santopinto, J. Phy. G24, 753 (1998). The curve shown is the calculation for 'potential 1' of that work.
- [27] N. Kaiser et al., Phys. Lett. B362, 23 (1995); Nuc. Phys. A612, 297 (1997).
- [28] N. Isgur and C. H. Llewellyn Smith, Phys. Rev. Lett. 52, 1080 (1984); A. V. Radyushkin, Nucl. Phys. A527, 153c (1991).
- [29] The angular distribution data are available upon request; please contact C. S. Armstrong.

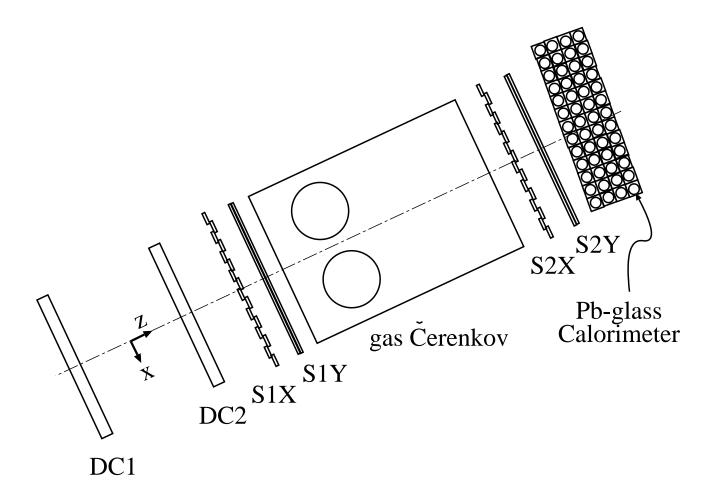
- FIG. 1. A plan view of the Hall C end station at Jefferson Lab. The electron beam enters from the left, and the scattering takes place in the cryogenic target placed in the beamline. In this experiment, outgoing particles were detected by two magnetic spectrometers: the Short-Orbit Spectrometer (SOS) was used to detect electrons and the High-Momentum Spectrometer (HMS) was used to detect protons.
- FIG. 2. A side view of the HMS detector stack, as seen from the door of the detector hut. The detected particles travel from left to right (along positive z).
- FIG. 3. The response of the SOS calorimeter and Čerenkov for events of a typical data run. The calorimeter response $E_{\rm cal}$ is the total energy deposited normalized to the particle momentum, while the Čerenkov response $N_{\rm p.e.}$ is the number of photo-electrons detected. The events at $N_{\rm p.e.}=0$ are π^- (note the peak at $E_{\rm cal}\approx 0.25$). The events at $N_{\rm p.e.}>0$, $E_{\rm cal}>0.7$ are electrons. The events at $N_{\rm p.e.}>0$, $E_{\rm cal}\approx 0.3$ are caused by π^- that produced knock-on electrons that triggered the Čerenkov. Note that the z axis is on a log scale.
- FIG. 4. Velocity from time of flight ($\beta_{\rm HMS}$) and coincidence time (the difference in time of arrival for the two spectrometers) for events of a typical data run. The band of events at $\beta_{\rm HMS} \approx 1$ are π^+ , while those at $\beta_{\rm HMS} \approx 0.8$ are protons. The real proton coincidences are at t=0 ns, and the nominal 2 ns radio frequency structure of the beam is visible in the adjacent accidental peaks. The low- $\beta_{\rm HMS}$ tail emanating from the real coincidence peak is most likely due to protons undergoing interactions in the detectors after the drift chambers.
- FIG. 5. A plot of M_x^2 for one kinematic setting. The peak at $M_x^2 \approx 0.3~({\rm GeV}/c^2)^2$ corresponds to undetected η mesons in the final state (the peak at $M_x^2 \approx 0.02~({\rm GeV}/c^2)^2$ corresponds to π^0 , the subject of Ref. [10]). Note the presence of the multi-pion background as well as the radiative tail extending to the right of the η peak.
- FIG. 6. Fits to the M_x^2 distribution for several typical $(\cos \theta_{\eta}^*, \phi_{\eta}^*)$ bins, one kinematic setting.
- FIG. 7. Results of background fits for several typical kinematic settings. Data are on the left and the corresponding Monte Carlo result is on the right. Each figure shows the integration of sixty individual $(\cos\theta_\eta^*\,,\,\phi_\eta^*)$ bins and their respective fits (like those shown in Figure 6). The solid line is the sum of the background and peak fits; the dashed line shows the background only. The lines at the bottom of the data plots show the small contribution from the accidental coincidence and HMS collimator backgrounds.
- FIG. 8. Angular distributions for the $Q^2=3.6~({\rm GeV}/c)^2$ data. Each plot shows the $\cos\theta_\eta^*$ distribution for a single $(W,\,\phi_\eta^*)$ bin. The rows correspond to different bins in W, the columns to different bins in ϕ_η^* . Data corresponding to $\phi_\eta^*=\pm90$ degrees are not shown; the out-of-plane experimental coverage was complete only for the lowest W bin (where the data looked similar to that in the ϕ_η^* bins shown here), and was almost nonexistent at higher W. The lines are S-wave fits to the data.

FIG. 9. Fit 1 to $\sigma_{\rm res}(W)$ for the two Q^2 points of this work (errors on the data are statistical only). Note the presence of the $p\eta$ threshold. The inset shows the W-dependence of this cross section as measured by the present work (solid line, $\Gamma_R = 154$ MeV), Ref. [13] (dashed line, $\Gamma_R = 203$ MeV), and Ref. [14] (dotted line, $\Gamma_R = 68$ MeV). The curves in the inset have been normalized to the same magnitude.

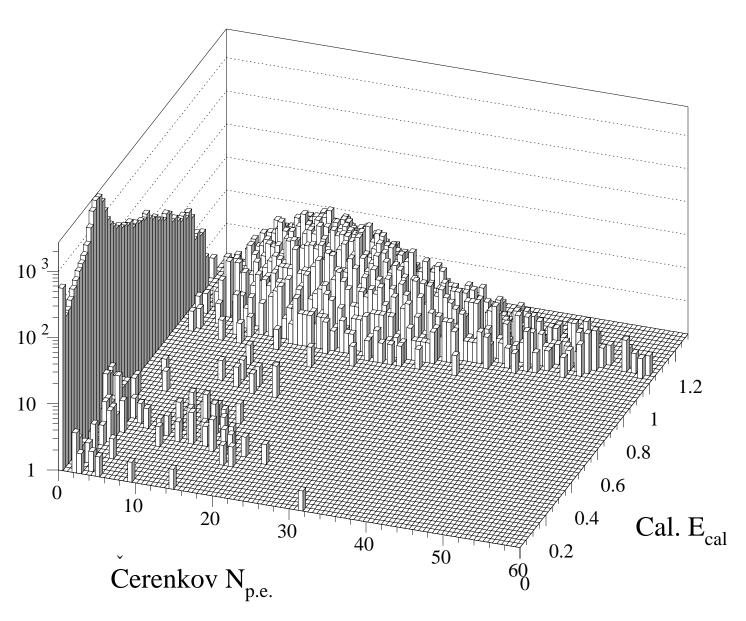
FIG. 10. The helicity amplitude $A_{1/2}^p(Q^2)$ of the $S_{11}(1535)$, measured via $e\,p \to e'p\,\eta$, together with some theoretical predictions. The data points ([13,14,21–25] and the present work) were calculated using $\Gamma_R=154$ MeV, $b_\eta=0.55$, and the parameterization of R referenced in the text. The errors shown on previous data are statistical only. The errors shown for the present work include both statistical and systematic uncertainties, with the exceptions noted in the text. The theoretical curves of Refs. [3–6,26] are based on variants of the CQM. The curve from Ref. [7] is the result of a pQCD calculation. The curve from Ref. [17] is a fit to inclusive data.

FIG. 11. The quantity $Q^3A_{1/2}^p(Q^2)$ for the $S_{11}(1535)$. The dot-dashed line is an exponential fit to the cross section given by the two points of the present work $(\sigma_{\rm res}=16.5\ {\rm exp}\,[-0.565\,Q^2]\ \mu{\rm b},$ where Q^2 is in [(GeV/c)^2]), and the solid line is a fit to inclusive data (as in Figure 10). The errors that are shown, and the assumed values for Γ_R , b_η , and R, are the same as in Figure 10.

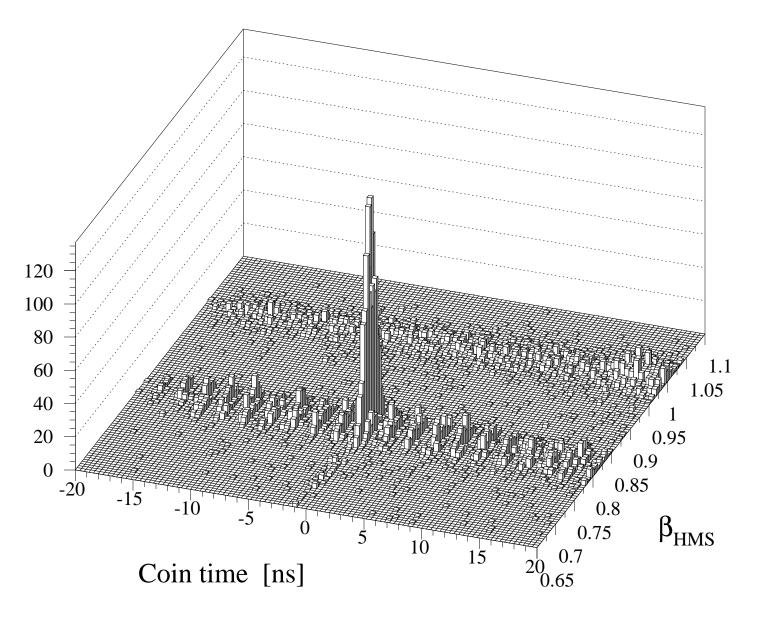


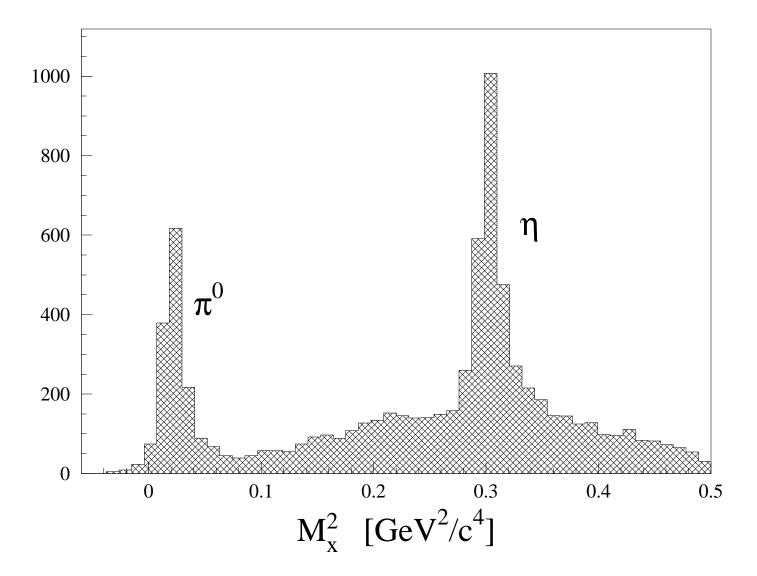


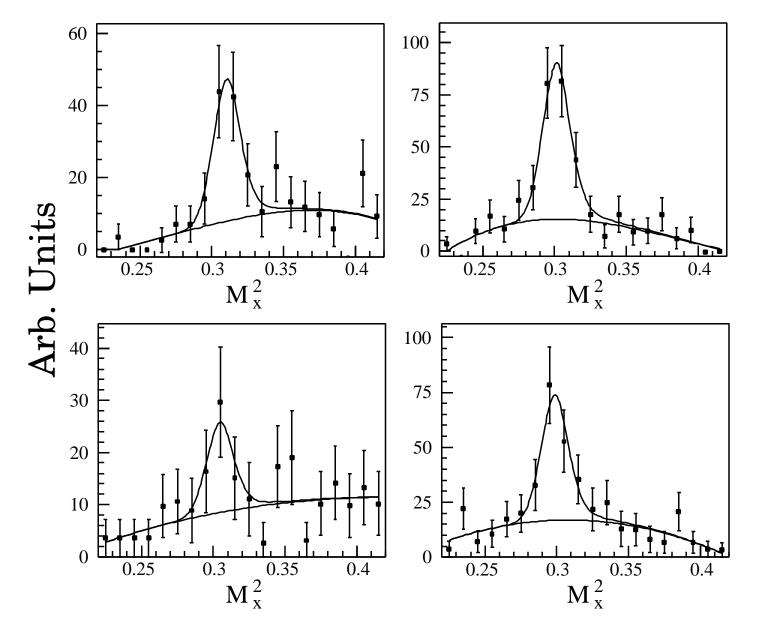
SOS Particle ID



HMS Particle ID and Coincidence Time







$Q^2 = 2.4 (GeV/c)^2$

